This is an open access article published under a Creative Commons Non-Commercial No Derivative Works (CC-BY-NC-ND) Attribution License, which permits copying and redistribution of the article, and creation of adaptations, all for non-commercial purposes.

ACS AUTHORCHOICE

ACS APPLIED MATERIALS & INTERFACES

Research Article

Cite This: ACS Appl. Mater. Interfaces 2020, 12, 200−208

www.acsami.org

3D Printing of Large Areas of Highly Ordered Submicron Patterns for Modulating Cell Behavior

M. Nouri-Goushki,*,† M. J. Mirzaali,† L. Angeloni,† D. Fan,‡ M. Minneboo,† M. K. Ghatkesar,‡ U. Staufer,‡ L. E. Fratila-Apachitei,† and A. A. Zadpoor†

†Department of Biomechanical Engineering and ‡Department of Precision and Microsystems Engineering, Faculty of Mechanical, Maritime, and Materials Engineering, Delft University of Technology (TU Delft), Mekelweg 2, 2628 CD, Delft, The Netherlands

ABSTRACT: Fabricating large areas of geometrically complex and precisely controlled topographies is required for the studies of cell behavior on patterned surfaces. Direct laser writing (DLW) is an advanced 3D-fabrication technique, which facilitates the manufacturing of structures within various scales (from a few hundred nanometers to millimeters). However, this method requires improvements in the accuracy and reproducibility of the submicron and nanoscale features that are printed over a large area. Here, we present a scheme to both improve the uniformity of the printed submicron patterns and decrease the printing time. The effects of various processing parameters (*e.g.*, laser power and writing field) on the dimensions and uniformity of submicron pillars as well as on their Young's modulus and surface wettability were assessed. Decreasing the writing field to 33 × 33 μm^2 significantly improved the uniformity of submicron pillars that were printed over an area of 4 mm^2 in a single-step process. Preosteoblast cells (MC3T3-E1) were used to assess the cytocompatibility of the used material (IP-L780 resin) with a focus on cell morphology, cell proliferation, cytoskeletal organization, and the elastic modulus of the cells. The cells cultured for 2 days on the submicron pillars showed a polarized shape and a higher Young's modulus of the area corresponding to the nucleus relative to those cultured on flat surfaces. Taken together, the results of the current study clearly show that the submicron patterns created using DLW are both cytocompatible and could modulate the morphology and mechanical properties of cells. This work paves the way for direct printing of submicron features with controlled Young's moduli over large areas in a single-step process, which is necessary for systematically studying how such patterns modulate cellular functions.

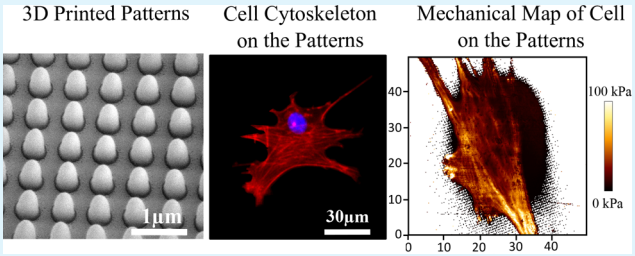

KEYWORDS: *Direct laser writing, topography, cell-surface interaction, 3D printing, submicron pillars, Young's modulus*

1. INTRODUCTION

Controlling cellular processes such as cell migration, proliferation, and differentiation is required for guiding and modulating tissue formation and regeneration.[1−4] In naturally occurring systems, the micro- and nanotopography of the extracellular matrix (ECM) plays an important role in this regard.[5−7] Mimicking the small-scale topography of the ECM and assessing the resulting cell−surface interactions are, therefore, necessary when developing novel biomaterials.[8−12] Indeed, recent studies have shown that nanoscale topographical features incorporated onto biomaterial surfaces could be used to guide the differentiation of stem cells toward the osteogenic lineage[13−15] and kill bacteria that may otherwise cause biomaterial-associated infections.[16,17] Achieving the desired effects is, however, often contingent on decorating the entire surface of (usually porous) biomaterials with precisely defined and geometrically complex nanopatterns.[6]

Fabricating porous biomaterials whose surface is covered by such types of nanopatterns remains a major unsolved challenge due to the inherent incompatibilities existing between the technologies required for the freeform fabrication of a complex porous structure and those required for freeform surface nanopatterning.[18] In fact, there is 5−6 orders of magnitude of difference between the length scale of the required nanopatterns (10−500 nm[13]) and that of the microarchitecture of the scaffold (10−900 μm[19]) used for bone implants. On one hand, no single freeform fabrication technique could create precisely controlled structures over such a wide range of length scales. On the other hand, combining multiple techniques is not feasible given the huge internal surface of porous biomaterials that cannot be reached once they have been fabricated. To put this technical challenge in perspective, it is worth reviewing the length scales that can be achieved by different types of 3D printing techniques. On the side of large length scales, the techniques based on material extrusion (e.g., fused deposition modeling[20]), powder bed fusion processes[21] (e.g., selective laser sintering[22,23] and electron beam melting[24]), and material jetting (e.g., inkjet technology[25−27]) could achieve length scales between 250 μm and 1 mm. Stereolithography can reach somewhat higher resolutions (i.e., down

Received: September 25, 2019
Accepted: December 3, 2019
Published: December 3, 2019

Downloaded via 207.241.233.138 on November 2, 2020 at 10:00:39 (UTC).
See https://pubs.acs.org/sharingguidelines for options on how to legitimately share published articles.

to 10 μm) while being capable of manufacturing large structures.[28] On the side of smaller length scales, electron beam induced deposition[29] could be used for freeform fabrication of structures with feature sizes between 10 nm and a few micrometers.[30]

A notable exception to the above-mentioned rule is direct laser writing (DLW) working on the basis of two-photon polymerization (2PP).[31] Although not capable of covering the entire range of the desired length scales, it covers a significant part of that range with features sized as small as 200 nm and as large as 100 mm.[32,33] Fine-tuning this technique to its limits has even allowed sub-20 nm feature sizes.[34] 2PP is therefore ideally positioned to address the challenge of freeform fabrication of nanopatterned porous biomaterials.

Incapability of tuning the defined geometries, particularly at high spatial resolutions and over specially large areas, has restricted the investigations of the effects of nanofeatures on the cellular behavior.[14] Even though DLW is a promising technology to fulfill these requirements, controlling this process over such a large range of length scales, to combine high enough speeds with high enough accuracy and repeatability, is technically extremely challenging. In fact, even submicron and nanoscale patterning of large surface areas has not been sufficiently addressed before. In a previous study,[35] we demonstrated that the application of the piezo-mode DLW for the submicron patterning of large surface areas is associated with both a long printing time and high levels of inaccuracy (i.e., nonuniformity) of the resulting pillars. Here, we followed an alternative DLW configuration (the so-called galvo-mode) for upscaling the area of patterned surfaces while decreasing the printing time and enhancing the uniformity of the fabricated features. Furthermore, we studied how different processing parameters influence the geometrical and mechanical properties of the resulting patterns. Finally, we created large patterned surface areas and studied the effects of patterns on the morphology, proliferation, and mechanical properties of preosteoblast cells.

2. MATERIALS AND METHODS

2.1. Fabrication of the Patterns. The geometry of individual pillars (diameter = 200 nm, height = 700 nm) was imported as a standard tessellation language (STL) file into a job preparation software (Describe, Nanoscribe, Germany). Describe then produced a general writing language (GWL) file from that STL file. The GWL code was modified to upscale the submicron pillars (pitch = 700 nm) so that they covered a large area of 4 mm^2. The file was then imported into the Photonic Professional GT machine (Nanoscribe, Germany) for 2PP exposure. The machine was equipped with a femtosecond (fs) laser source that emitted 100 fs pulses at 80 MHz with a wavelength of 780 nm (Figure 1a).

The galvo writing mode and conventional configuration were used for patterning similar surface areas (Figure 1aI). A droplet of photoresist (IP-L780, Nanoscribe, Germany) was placed atop a borosilicate coverslip (Nanoscribe, Germany). The laser beam was then focused within the resin using a 63× microscope objective (numerical aperture [NA] = 1.4). After exposing, the development process was performed in propylene glycol monomethyl ether acetate (PGMEA, Sigma-Aldrich, Germany) for 25 min followed by 5 min rinsing in isopropyl alcohol (IPA) (Sigma-Aldrich, Germany) and subsequent blow-drying with air.

The submicron pillars were written using a scanning speed of 1200 μm/s. The effects of different laser powers (Lp: 12−21% of the mean power value at the objective aperture) on the dimensions and Young's moduli of the submicron pillars were assessed accordingly. The water contact angle measurements, the measurement of the detachment force of the pillars, and the cell experiments were then performed on the pillars created using a Lp of 21%.

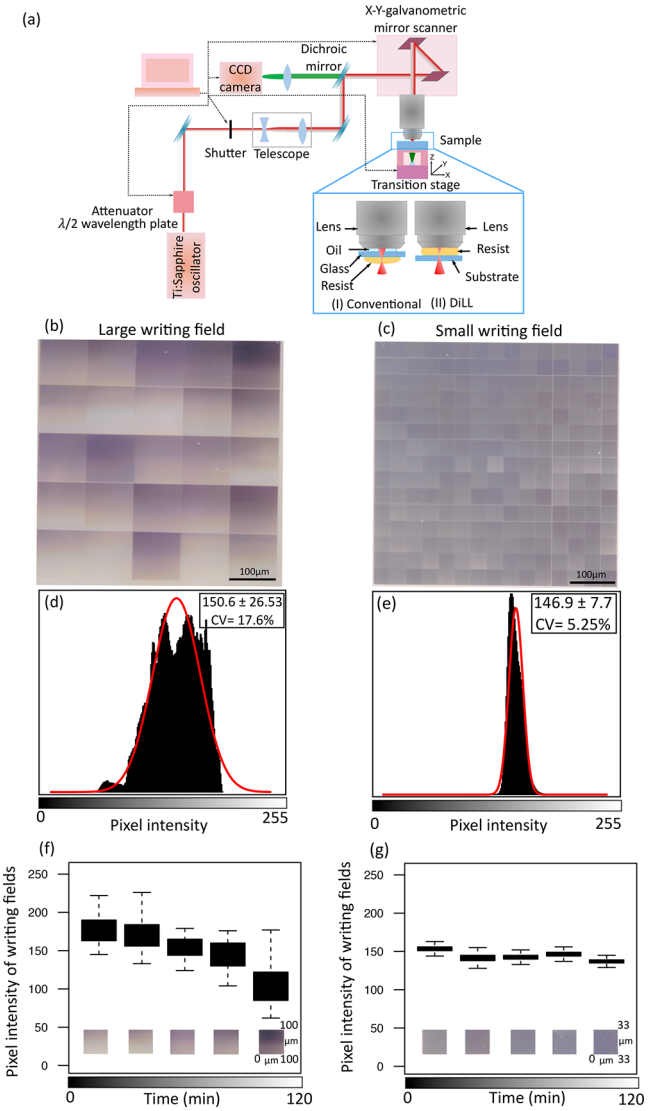

Figure 1. Schematic drawing of the applied nanoscale 3D printing technique and the results of the writing field optimization process. (a) Schematic illustration of the 2PP system: the system consists of an exposure source (Ti Sapphire laser, pulse duration: 100 fs, wavelength: 780 nm, and repetition rate: 80 MHz) and a $\lambda/2$ wavelength plate and a cube polarizer for attenuating the laser power. The beam is expanded by a telescope and positioned into the resin either by the galvo scanner or the 3D transition stage. The CCD camera placed behind a dichroic mirror displays the printing process online. Either a conventional (I) or a Dill configuration (II) can be used for the printing process. (b,c) Optical microscopy images showing the uniformity of the DLW submicron pillars for writing fields of 100 × 100 μm^2 and 33 × 33 μm^2, respectively. (d,e) Frequency distribution of the pixel intensity obtained from optical images (subfigures b, c). Gaussian functions (red curves) were fitted to the pixel intensity data. (f,g) Pixel intensity of large (100 × 100 μm^2) and small (33 × 33 μm^2) writing fields vs the printing time.

2.2. Microscopic Characterization of the Patterns. The features resulting from the writing processes were characterized using a scanning electron microscope (SEM, Nova Nano Lab 650 dual beam system, FEI company, USA) before and after culturing cells on them. All samples were gold-sputtered using a sputter coater (JFC-1300, JEOL, Japan) for 60 s (coating thickness ≈ 5 nm) before imaging. Two-dimensional maps of the patterned areas were also

DOI: 10.1021/acsami.9b17425
ACS Appl. Mater. Interfaces 2020, 12, 200−208

acquired by an optical microscope (Keyence Digital Microscope VHX-6000, USA) to check the uniformity of the patterns. The dimensions of 100 different pillars were quantified from SEM images using ImageJ (http://rsb.info.nih.gov/ij/index.html).

2.3. Contact Angle Measurement. A drop shape analyzer (KRUSS DSA100, Germany) was used to measure the wettability of the patterned surfaces. Deionized water droplets (volume = 2 μL) were placed on the nonpatterned (borosilicate coverslips) and patterned surfaces. The contact angle was measured after 5 s (three measurements per specimen). The specimens were cleaned with IPA and dried with nitrogen gas prior to the measurements.

2.4. Mechanical Characterization. *Young's modulus.* The mechanical experiments reported here were performed using an atomic force microscope (AFM) (JPK Nanowizard 4, Berlin, Germany) while the corresponding data postprocessing was carried out with the JPK SPM data processing software (JPK instruments, v 6.1, Berlin, Germany).

The Young's moduli of a number of large deposits of the IP-L780 resin (i.e., pillars with a diameter of 1 μm and height of 500 nm) written at different laser powers were measured using the quantitative imaging (QI) mode, and an NM-TC probe (Bruker, Billerica, USA) with a nominal spring constant of 350 N/m. The deflection sensitivity of the cantilever was calibrated on a sapphire surface using the contact method and resulted in a value of 21.33 nm/V. The spring constant of the probe was assumed equal to the nominal value, and the relative method of calibration was applied to estimate the corresponding tip radius. A polystyrene sample with a nominal Young's modulus of 3 GPa was used as the reference material. The tip radius was then adjusted to make the measured Young's modulus of the reference sample equal to the nominal value at an indentation depth of 10 nm. A Poisson's ratio of 0.4 was assumed. A tip radius of 10 nm was found to result in a Young's modulus of 3.1 GPa for the polystyrene. Then, a constant set point force of 500 nN was applied to each sample in order to obtain an indentation depth of 10 nm. The Hertz's contact mechanics model was used to calculate, from the force−distance curves recorded in each point of the scanned area, the Young's modulus corresponding to each scanned point. The Young's modulus of 3 pillars for each 2PP printing condition was calculated, from the Young's modulus map, as the average values in a selected area corresponding to the top of the pillar.

Detachment Force of Pillars. The measurement of the detachment force of the pillars was performed using the same instrument and a NCHV probe (Bruker) with a nominal spring constant of 40 N/m, a nominal cantilever length of 115 μm, a thickness of 3.5 μm, and a tip height of 10 μm. The thermal noise calibration technique was used to measure the spring constant and the sensitivity of the probe, which were found to be, respectively, 38.26 N/m and 19.51 nm/V.

Areas of 20 μm × 20 μm (containing 13 pillars) were scanned successively in QI mode, with a pixel time of 18 ms, a Z length of 500 nm, and increasing values of the lateral force (from 2 μN to 5.5 μN) obtained by setting increasing values of the set point deflection (from 52 to 130 nm). The number of detached pillars corresponding to each level of applied force and the eventual changes in the morphology of the scanned pillars due to the applied force were evaluated by acquiring, after the application of each force value, a QI image with a low set point deflection (i.e., 1.5 nm).

The scanning direction was chosen such that the contact between the probe and the pillars occurred on one of the lateral faces on the front of the pyramidal AFM tip. The force (F_N) applied to the pillar is therefore directed along the normal to that surface.

The magnitude of the lateral component of the force applied to the pillar was calculated as

$$F_{lat} = \sqrt{F_{N,x}^2 + F_{N,y}^2} \tag{1}$$

where

$$F_{N,x} = F_N \cos\beta \cos\gamma \tag{2}$$

$$F_{N,y} = F_N \sin\beta \cos\gamma \cos\varphi - F_N \sin\gamma \sin\varphi \tag{3}$$

are the components of F_N along the two orthogonal directions (x and y) normal to the axis of the pillar (z). From the beam theory and after applying the geometry considerations, F_N, can be calculated as

$$F_N = \frac{k^* d_z}{\sin\gamma - \frac{3}{2}\frac{\left(h_{tip} + \frac{t}{2}\right)}{L}\sin\beta\cos\gamma} \tag{4}$$

where d_z is the set point deflection of the cantilever, k^* is the equivalent spring constant of the system cantilever + pillar, β is the half front angle of the tip (measured by SEM imaging of the probe), and γ is the angle of inclination of the tip wall with respect of its axis and is calculated as $\gamma = \arctan\left(\frac{l_{tip}\sin\beta}{h_{tip}}\right)$ where l_{tip} is the length of the tip (measured by SEM imaging of the probe). The other parameters include φ that is the tilting angle of the cantilever holder with respect to the horizontal direction (10° in JPK systems), h_{tip} that is the height of the tip, and t that is the thickness of the cantilever. The parameter k^* was measured as the slope of the contact region of the force−distance curves when the tip was in contact with the pillar (e.g., at a scan point before pillar failure).

2.5. Cell Experiments. *Cell Seeding and Culture.* Preosteoblast cells (MC3T3-E1, Sigma-Aldrich, Germany) at passage 11 were seeded on the control (borosilicate coverslips) and patterned surfaces (n = 4) at a concentration of 25 × 10^3 cells/mL. The samples were incubated in the alpha minimal essential medium (α-MEM without ascorbic acid: supplemented with 10% (v/v) fetal bovine serum (FBS), 1% (v/v) penicillin-streptomycin (10 000 units/mL), pH = 7.5, Life Technologies, USA) for 2 or 4 days (37 °C, 5% CO_2). The medium was refreshed after 2 days.

Cytoskeleton Staining. Actin staining was performed on days 2 and 4. Therefore, the cells were washed two times with phosphate-buffered saline (PBS, Sigma-Aldrich, Germany) and then fixated in 4% formaldehyde/PBS (Sigma-Aldrich, Germany) at room temperature for 10 min. Then, the samples were rinsed with PBS and the cells were permeabilized with 0.5% Triton/PBS (Sigma-Aldrich, Germany) at 4 °C for 15 min. The specimens were then incubated in 1% bovine serum albumin (BSA)/PBS (Sigma-Aldrich, Germany) for 5 min at 37 °C followed by the addition of rhodamine conjugated phalloidin (1:1000 in 1% BSA/PBS, Life Technologies, USA) and incubation for 1 h at 37 °C. Subsequently, the samples were washed 3 times for 5 min with 0.5% Tween/PBS (Sigma-Aldrich, Germany) followed by washing with PBS for 5 min. Next, 70 μL Prolong gold (containing 4′,6-diamidino-2-phenylindole (DAPI), Life Technologies, USA) were added to the cells and the samples were mounted on glass slides and observed using a fluorescence microscope (ZOE fluorescent cell imager, Bio-Rad, USA).

Consequently, the stained specimens were rinsed 2 times with distilled water for 5 min. The cells were then dehydrated in a series of graded ethanol/PBS solutions (Sigma-Aldrich, Germany) as follows: 15 min in 50%, 20 min in 70%, and 20 min in 96%. The specimens were allowed to dry overnight and were gold sputtered for SEM imaging.

Image Analysis. The images of the stained cells on days 2 and 4 were processed using ImageJ. First, the image overlay of the fluorescently stained F-actin and nucleus was split into channels to separate the nucleus from the F-actin network. The grayscale nucleus and F-actin images were thresholded to produce binary nucleus and F-actin images, respectively. The cell density was determined through counting the nuclei observed in four different 1 mm^2 areas of each specimen. The area of the cells was quantified through measuring the actin area of 150 single cells on four different 1 mm^2 area of the specimens. By fitting an ellipse to the actin area of each cell, which can be performed through particle analyzing in ImageJ, the degree of anisotropy (DA) was calculated using the following equation:

$$DA = 1 - d_2/d_1 \tag{5}$$

where d_2 and d_1 are the minor and major diameters of the fitted ellipse (ImageJ, BoneJ2, https://github.com/bonej-org/BoneJ2/tree/bonej-6.1.1). DA = 0 means the cell is fully isotropic and does not have

DOI: 10.1021/acsami.9b17425
ACS Appl. Mater. Interfaces 2020, 12, 200−208

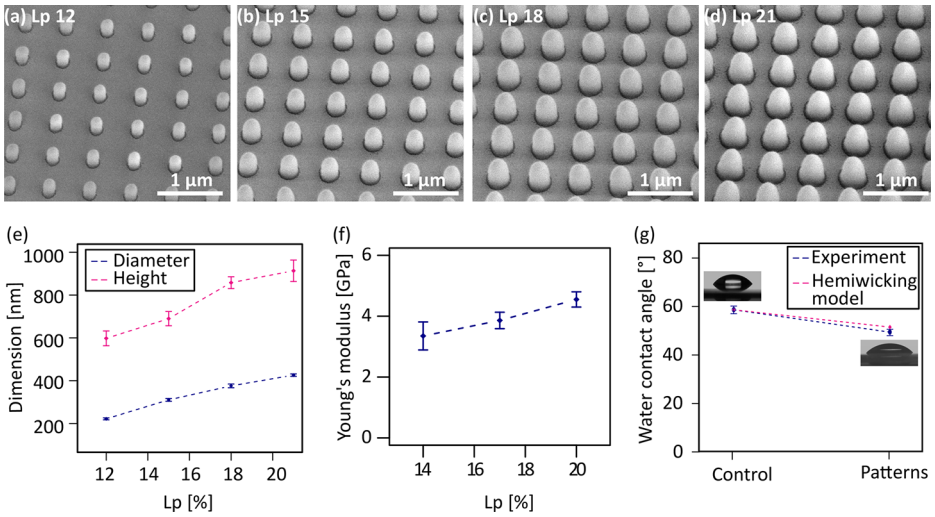

Figure 2. Submicron pillars characterization. (a−d) SEM images of the submicron pillars printed using laser powers of 12%, 15%, 18%, and 21%, respectively. (e) Dimensions of the submicron pillars as a function of the laser power. (f) Young's modulus of the submicron pillars as a function of laser power. (g) Experimental and theoretical measurements of the water contact angle on the flat and patterned surfaces (Lp = 21%). The dotted lines are included to guide the eye.

directionality, while $DA \sim 1$ indicates a strong preferential orientation in the cells.

AFM Characterization. The morphology and mechanical properties (Young's modulus) of living cells at day 2 were characterized using an AFM (JPK Nanowizard 4, Berlin, Germany). The JPK Petri dish heater was used to maintain cells at 37 °C during the measurements. A MLCT-Bio probe (type B, rectangular) with a nominal spring constant of 0.02 N/m and a tip having the shape of a square-based pyramid (nominal front, side, and back angles of 35°) was used. The probe was calibrated using thermal noise method, resulting in a sensitivity of 23.29 nm/V and a spring constant of 0.017 N/m. A set-point force of 1 nN, a pixel time of 18 ms, and a Z length of 1.5 μm were used for the measurements on each cell. The Young's modulus was calculated by fitting the force−distance curves obtained in each point of the scanned area to the Hertz-Sneddon model considering a square-based pyramid as the indenter. The maximum height of the cells was measured in the region corresponding to the nucleus. The reported values of the Young's modulus are the average of the Young's moduli measured in selected areas corresponding to the cell nucleus.

2.6. Computational Models. A nonlinear finite element solver (Abaqus 6.14) was used for the numerical simulations of the reaction force of the pillar under bending. The 3D geometries of a pillar and a glass plate were first created in the finite element program. Two different linear elastic material models were assigned to the pillar (E_{np} = 4.55 GPa, ν_{np} = 0.4) and the glass plate (E_g = 63 GPa, ν_g = 0.2[36]). The Young's modulus of the pillar (printed with Lp = 21%) was already measured through a nanomechanical system and explained in more details in section 2.4. The pillar was assumed to be attached to its glass base. Therefore, a tie constraint was used at their interface. A 20-node quadratic brick element with hybrid mode formulation (C3D20H) was used to create the 3D mesh.

To apply the displacement-controlled boundary conditions, a reference point was defined at the top surface of the pillar, which was kinematically coupled to the corresponding nodes of that surface. Different displacements (up to 235 nm at which point the submicron pillars partially detached from substrate, as obtained from the SEM images of the cells) normal to the main axis of the pillar was applied to the reference point. The reference point was free to rotate in three directions. A clamped boundary condition was applied to the base plate to constrain the possible rigid body motions of the submicron pillar and base plate. The reaction force (along the direction of the applied displacement) at the reference point was calculated. We also performed a mesh sensitivity analysis for different minimum element sizes (i.e., 80, 60, 40, 20 nm). An element size equal to 20 nm led to <1% variations in the calculated value of the reaction force and was, therefore, used to obtain all of the results that are reported below.

3. RESULTS AND DISCUSSION

3.1. Pattern Fabrication. The 2PP technique can accurately manufacture microscale structures (i.e., with feature dimensions above one micron). The main challenge, therefore, is in printing submicron and nanoscale features with high precision over large areas of the surface.[34,35] One of the important parameters affecting the uniformity of DLW objects at these length scales is the writing field, which was assessed by the optical imaging of the arrays of pillars printed with two different field sizes and analyzing the contrast of the images obtained for each field (Figure 1b,c). By decreasing the writing field from 100 μm × 100 μm to 33 μm × 33 μm, the tilt and the astigmatism of the galvo scanning process were less pronounced, which led to more uniform pillars (Figure 1c). The variation in the pixel intensity shows the difference in the height of the printed pillars. The coefficient of pixel variation (i.e., CV = SD/mean) was 3 times smaller after optimizing the printing process (i.e., decreased from 17.6% to 5.25%, Figure 1d,e), meaning that the procedure proposed in this study resulted in a multifold decrease in the variations observed in the height of the submicron pillars (Figure 1c,e). Furthermore, for the larger writing field (i.e., 100 μm × 100 μm), a decrease in the pixel intensity was observed with the printing time (Figure 1f), which shows an increase in the height of the pillars (the lower the intensity, the larger the height of the pillars). In addition, larger variations were observed within each field. On the other hand, for the smaller writing field (i.e., 33 μm × 33 μm), the pixel intensity inside various fields was more or less constant regardless of the printing time (Figure 1g), which suggests that the height of the pillars is uniform. In this study, the submicron patterns were uniformly reproduced over areas up to 4 mm^2. In terms of the printing time, the technique proposed here resulted in three times shorter printing times for the same area as compared to the piezo printing mode reported in our previous study.[35] Obviously, the printing time depends on the dimensions and density of the printed pillars,

DOI: 10.1021/acsami.9b17425
ACS Appl. Mater. Interfaces 2020, 12, 200−208

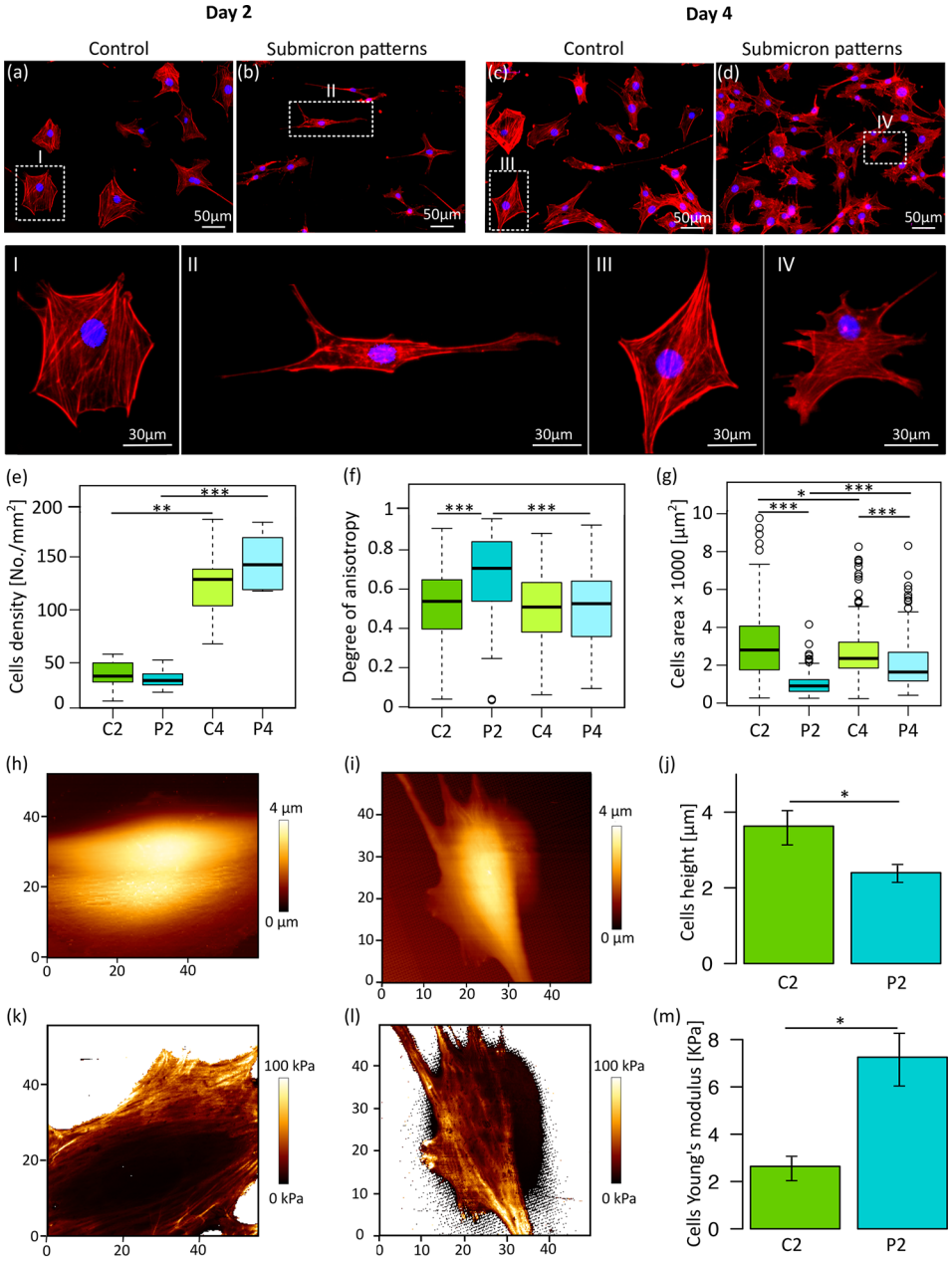

Figure 3. Fluorescence microscopy images of the MC3T3-E1 cells cultured on the flat control and patterned surfaces (a), (b) F-actin (red) and nucleus (blue) staining of cells on the control (i.e., glass) and patterned surface (Lp = 21%) on day 2. (c,d) F-actin and nucleus of the cells cultured on the control (i.e., glass) and patterned surfaces (Lp = 21%) on day 4. (I−IV) Magnified views of the indicated regions in a-d. (e−g) Cell density, degree of anisotropy, and F-actin area measured on the control (C2, C4) and patterned (P2, P4) surfaces on days 2 and 4, as determined from the fluorescence images. (h−j) AFM-measured morphological images of the cells cultured on the control and patterned surfaces on day 2 (h,i) and the values of the cells maximum height (j). (k−m) The AFM mechanical maps on the control and patterned surfaces on day 2 (k,l) and the values of the Young's modulus measured in the area corresponding to the nucleus (m). The Student's *t* test was used to compare the statistical significance of the differences between both groups. A *p* value below 0.05 was considered statistically significant (* denotes $p < 0.05$, ** denotes $p < 0.01$, *** denotes $p < 0.001$).

and the area to be patterned. For example, the printing time was 6−8 h for covering an area of 1 mm^2 with pillars whose diameter and height are presented in Figure 2e.

The laser power significantly influenced the dimensions of the pillars including both diameter and height (Figure 2a−e). Increasing the laser power will increase size of the volume around the focal point of the focused laser beam, where the intensity is high enough to initiate two-photon processes. This affects the feature dimensions on the submicron scale (i.e., feature sizes ≤1 μm). Therefore, to control the dimensions of such small features, fine-tuning of the printing parameters in general and the laser power in particular is needed. Figure 2e indicates how the diameter and height of pillars in the submicron range can be controlled through the adjustment of the laser power. As the laser power increased from 12% to 21%, the mean diameter of the submicron pillars almost doubled (from 222 to 426 nm) while their mean height increased from ∼600 nm to ∼900 nm (Figure 2e). The standard deviation of the diameter of the pillars was particularly low (i.e., 4−8 nm), while the pillars' height

DOI: 10.1021/acsami.9b17425
ACS Appl. Mater. Interfaces 2020, 12, 200−208

showed somewhat higher levels of variation (i.e., 30−50 nm) (Figure 2e). Furthermore, the small coefficient of variation in diameter and height (2% and 5%, respectively) for different laser powers underlined the reproducibility of the process. A proper selection of the laser power is therefore essential for the fabrication of pillars with controlled dimensions in the submicron to nanoscale range.

3.2. Mechanical Properties. An increase in the Young's modulus from 3.35 to 4.55 GPa was also observed for the used material (IP-L780) with increasing the laser power from 14% to 20% (Figure 2f). This could be explained by a higher degree of cross-linking and, thus, increased Young's modulus resulting from a higher laser power (at a constant writing speed).[37] The possibility to tune the Young's modulus of DLW material using the laser processing parameters and within the same single-step fabrication process can be of great utility when trying to manufacture 3D structures with gradient stiffnesses at microscale. It would, however, be increasingly more challenging to achieve the same with submicron features, because the laser power will affect both the Young's modulus and the size of the structures. That said, the dimensions of submicron patterns can be controlled even when the laser power and writing speed are kept constant (to ensure the Young's modulus remains unchanged).

3.3. Water Contact Angle. According to previous studies,[38,39] both chemical composition and geometric parameters affect the wettability of patterned surfaces. In this study, the contact angle decreased from 58 ± 1.35° (n = 6) on the nonpatterned substrate to 48.9 ± 2.29° (n = 6) on the patterned surface, indicating a shift toward hydrophilicity as a result of patterning (Figure 2g). This observation can be explained through the Hemiwicking's phenomenon[38] according to which a patterned surface can absorb the water droplet due to its surface roughness. Therefore, the water penetration propagates through pillars beyond the droplet and a liquid film forms over the surface. The Hemiwicking' phenomenon occurs when the contact angle of a nonpatterned surface (Young's angle = θ) is smaller than a critical value θ_c given by the following relationship:[38]

$$\cos\theta_c = (1 - \varphi_s)/(r - \varphi_s) \tag{6}$$

where ϕ_s is the density of the submicron pillars and r is the roughness factor on rough surfaces. The roughness factor is defined as the ratio of the rough surface area to that of the flat surface area (for a smooth surface r = 1, and for a rough surface r > 1). Approximating pillars as cylinders, for the square pillar arrays, ϕ_s and r are given as[38,40]

$$\varphi_s = \pi d^2/4p^2 \tag{7}$$

$$r = \frac{A_r}{A_f} = \frac{p^2 + 4 \times \left(\frac{\pi dh}{4}\right)}{p^2} = 1 + \pi dh/p^2 \tag{8}$$

Substituting the dimensions of the submicron pillars (d = 426 nm, h = 913 nm, p = 700 nm, p is defined as the distance between the center of two adjacent pillars) into eqs 6−8, yields ϕ_s = 0.3, r = 3.49, and θ_c = 77°. As θ_c is higher than the Young's angle (58°), the water contact angle on the submicron pillars can be calculated as[38]

$$\cos\theta^* = 1 - (1 - \varphi_s)\cos\theta \tag{9}$$

This equation accurately predicts both a theoretical contact angle (θ^* = 51°) that agrees with the experimental value of the contact angle (49°) and an increase in hydrophilicity that is also observed in our experiments (Figure 2g).

3.4. Response of MC3T3-E1 Cells to the 2PP Patterns. The pillars made with the highest laser power (i.e., Lp = 21%) were selected for the preliminary cell experiments, because they showed the highest Young's moduli (Figure 2f). Moreover, a stiffer substrate is known to stimulate the osteogenic differentiation of osteoprogenitor cells.[41] First, the MC3T3-E1 cells cultured on the patterned surfaces showed no signs of death indicating that the polymer is not cytotoxic for these cells and time of exposure. From the second day of culture, the cells residing on the nonpatterned surfaces developed a well-spread, polygonal morphology with areas around 3000 μm^2 (as determined from the actin cytoskeleton staining) (Figure 3a,c, I,III). Furthermore, the number of cells increased from day 2 to day 4 on this surface while cell morphology and degree of anisotropy did not change significantly (Figure 3a,c,e,f).

By comparison, the cells cultured on the patterned surfaces appeared highly polarized on day 2 with clear filopodia developed for attachment and significantly smaller cell area, resulting in higher anisotropy (Figure 3b, II, f, g). Over time, the cells grew in size and adopted a more well-spread stellate morphology on the patterned surfaces (Figure 3d, IV, g). Consequently, the degree of anisotropy of the cells significantly decreased from day 2 to day 4 on the patterned surfaces (Figure 3f). In addition, the proliferative capacity of the cells was found to be at least similar to that of the cells cultured on the nonpatterned surfaces, as indicated by the measurement of the cell density (Figure 3e). The actin fibers were oriented parallel to the stretching direction on both nonpatterned and patterned surfaces, but they were less organized on the patterned surfaces due to the stretching in all directions (stellate shape) (Figure 3d, IV).

The morphological analysis of living cells performed using AFM on day 2 revealed a number of other interesting findings. First, the heights of the cells cultured on patterned surfaces were lower as compared to the cells cultured on nonpatterned surfaces, confirming the highly polarized morphology of the cells interacting with the patterns (Figure 3h,i,j). In addition, for the cells interacting with the patterned surfaces, the presence of perinuclear actin cap fibers was observed in the mechanical maps (Figure 3l). This could contribute to the higher value of the Young's modulus (Figure 3l,m) measured in the area corresponding to the nucleus of these cells. By comparison, thicker and peripheral actin fibers were observed on the nonpatterned surfaces (Figure 3k,m).

A closer look at the cell−surface interface by SEM revealed that the cells' filopodia used the pillars as anchoring sites and that some of the pillars bent, especially at the local regions around the edge of the cells (Figure 4a−d). This implies that the cell adhesion forces differed locally, with possibly higher forces at the leading front than at the rear of the cell. Based on the SEM image analysis, the lateral displacement of the pillars by cells was estimated to be between 0 and 235 nm (Figure 4c,d). Our computational model of the pillars was then used to estimate the corresponding reaction force of the pillars given the measured Young's modulus of the material (Figure 4e). We found that forces around 2.5 μN corresponded to the maximum measured displacement. AFM nanomechanical experiments indicated detachment forces of the pillars from

DOI: 10.1021/acsami.9b17425
ACS Appl. Mater. Interfaces 2020, 12, 200−208

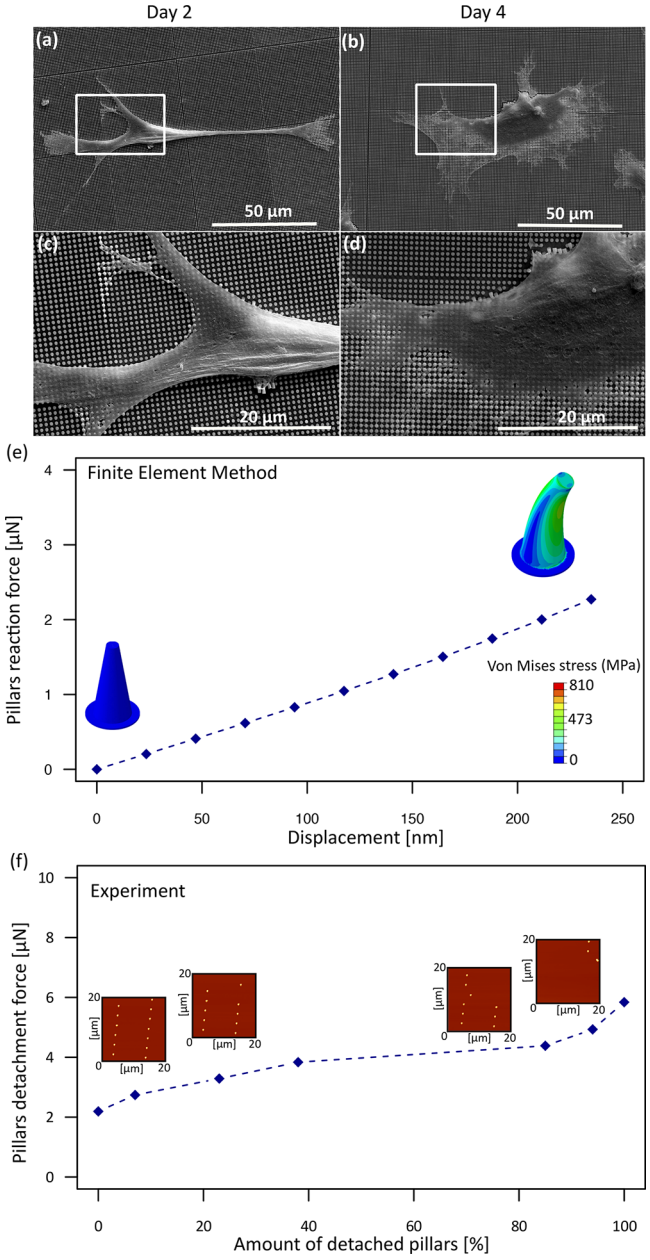

Figure 4. Cell–surface interactions. (a,b) SEM images of the cells cultured on the patterned surfaces (Lp = 21%) after 2 and 4 days, respectively. (c,d) Magnified views of the indicated regions in subfigures a and b. (e) Results of the computational model which represent the pillars reaction force (F) vs displacement. The inset figures visualize the von Mises stress distribution within the submicron pillars for lateral displacement of 0 and 235 nm. (f) AFM experimental results of submicron pillars detachment force. The bright dots in the micrographs represent the pillars remaining after the application of a certain force. This indicates that the pillars "peeled off" from the substrate, suggesting that the failure occurred at the interface between the substrate and the pillar.

the substrate in the range between 2.5 μN and 5.5 μN. Few completely detached pillars were actually visible around the edges of some cells (Figure 4c,d) indicating that those cells exerted forces ≥4 μN locally on some pillars. Further studies are required to exactly measure the adhesion force of the cells on the substrate. The adhesion of pillars to the substrate can be enhanced by increasing the diameter of the pillars, decreasing the height of the pillars, and increasing the interface distance during the printing process.[35]

These findings suggest that cells on the patterns initially required a period of adaptation to the surface but once attached, their migration, proliferation, and spreading were supported by the patterned surfaces probably with the contribution of the enhanced hydrophilicity of these surfaces.[35,42−44] The effects of different cell morphologies observed at the early time points on the later cellular functions such as osteogenic differentiation need to be further investigated.

The ability of the presented methodology to generate large areas covered by submicron patterns with a controlled height, diameter, interspacing, and Young's modulus in a single-step process is unique among 3D printing techniques. Furthermore, the possibility of creating 3D structures decorated with such surface nanopatterns allows us to approach the complexity of stem cell niche with regard to the extracellular matrix characteristics. Together with the shown cytocompatibility of the used resins for mouse preosteoblasts (IP-L780 resin, in this study) and human stem cells (IP-Dip resin, in our previous study[35]), the 2PP process enables the systematic studies of the effects of these complex structures on cellular functions.

4. CONCLUSIONS

In summary, we presented a comprehensive study on an advanced 3D printing method for generation of patterns with controlled morphology and mechanical properties in a single-step process, relevant for modulating cell behavior. Our results led to an optimized 2PP method for a fast and improved reproducibility of DLW submicron features over large areas by modifying the writing mode and field while optimizing the laser power of the DLW system. More specifically, we could achieve a 3-fold decrease in the printing time and uniform patterns (coefficient of variation ∼5%) over an area of 4 mm^2. Increasing the laser power not only increased the polymerized volume but also resulted in a higher Young's modulus of the structure. Both experimental and simulation data showed that forces in the range of 2.5−5.5 μN could detach the pillars from the substrate. The hydrophilicity of the surface was enhanced by patterning. Importantly, our cell experiments confirmed that the IP-L780 resin used here is compatible with MC3T3-E1 cells. The surface patterns significantly influenced the morphology of these cells as compared to the nonpatterned surfaces while proliferation showed a similar trend over the 4 days of culture. In addition, the Young's modulus corresponding to the nucleus area of the cells cultured on the patterned surfaces for 2 days was significantly higher than of those cultured on the nonpatterned surfaces. This study indicates that the 2PP process provides unique possibilities for studying the effects of highly controlled submicron patterns on the bone tissue regeneration process.

■ AUTHOR INFORMATION

Corresponding Author

*E-mail: m.nourigoushki@tudelft.nl; mhd.nouri71@gmail.com. Tel.: +31-685267905.

ORCID

M. Nouri-Goushki: 0000-0003-1665-9144
L. E. Fratila-Apachitei: 0000-0002-7341-4445
A. A. Zadpoor: 0000-0003-3234-2112

DOI: 10.1021/acsami.9b17425
ACS Appl. Mater. Interfaces 2020, 12, 200−208

Notes

The authors declare no competing financial interest.

■ REFERENCES

(1) Cha, C.; Liechty, W. B.; Khademhosseini, A.; Peppas, N. A. Designing Biomaterials to Direct Stem Cell Fate. *ACS Nano* **2012**, *6* (11), 9353−9358.

(2) Lutolf, M. P.; Gilbert, P. M.; Blau, H. M. Designing Materials to Direct Stem-Cell Fate. *Nature* **2009**, *462* (7272), 433−441.

(3) Yin, S.; Zhang, W.; Zhang, Z.; Jiang, X. Recent Advances in Scaffold Design and Material for Vascularized Tissue-Engineered Bone Regeneration. *Adv. Healthcare Mater.* **2019**, *8* (10), 1801433.

(4) Cavalcanti-Adam, E. A.; Missirlis, D. Nanoscale Control of Cell Behavior on Biointerfaces. *Biomimetic Approaches Biomater. Dev.* **2012**, 213−236.

(5) Dalby, M. J.; Gadegaard, N.; Oreffo, R. O. Harnessing Nanotopography and Integrin-Matrix Interactions to Influence Stem Cell Fate. *Nat. Mater.* **2014**, *13* (6), 558−569.

(6) Brammer, K. S.; Choi, C.; Frandsen, C. J.; Oh, S.; Jin, S. Hydrophobic Nanopillars Initiate Mesenchymal Stem Cell Aggregation and Osteo-Differentiation. *Acta Biomater.* **2011**, *7* (2), 683−690.

(7) Rizwan, M.; John, W. T.; Nori, A.; Leong, K. W.; Yim, E. K. Cell-Substrate Interactions. In *Principles of Regenerative Medicine*; Elsevier: 2019; pp 437−468.

(8) Santos, E.; Orive, G.; Hernández, R. M.; Pedraz, J. L. Cell-Biomaterial Interaction: Strategies to Mimic the Extracellular Matrix. In *On Biomimetics*; IntechOpen: 2011.

(9) Resende, R. R.; Fonseca, E. A.; Tonelli, F. M.; Sousa, B. R.; Santos, A. K.; Gomes, K. N.; Guatimosim, S.; Kihara, A. H.; Ladeira, L. O. Scale/Topography of Substrates Surface Resembling Extracellular Matrix for Tissue Engineering. *J. Biomed. Nanotechnol.* **2014**, *10* (7), 1157−1193.

(10) Janson, I. A.; Putnam, A. J. Extracellular Matrix Elasticity and Topography: Material-Based Cues that Affect Cell Function via Conserved Mechanisms. *J. Biomed. Mater. Res., Part A* **2015**, *103* (3), 1246−1258.

(11) Lord, M. S.; Foss, M.; Besenbacher, F. Influence of Nanoscale Surface Topography on Protein Adsorption and Cellular Response. *Nano Today* **2010**, *5* (1), 66−78.

(12) Kulangara, K.; Leong, K. W. Substrate Topography Shapes Cell Function. *Soft Matter* **2009**, *5* (21), 4072−4076.

(13) Dobbenga, S.; Fratila-Apachitei, L. E.; Zadpoor, A. A. Nanopattern-Induced Osteogenic Differentiation of Stem Cells-A Systematic Review. *Acta Biomater.* **2016**, *46*, 3−14.

(14) Pedrosa, C. R.; Arl, D.; Grysan, P.; Khan, I.; Durrieu, S. p.; Krishnamoorthy, S.; Durrieu, M.-C. Controlled Nanoscale Topographies for Osteogenic Differentiation of Mesenchymal Stem Cells. *ACS Appl. Mater. Interfaces* **2019**, *11* (9), 8858−8866.

(15) McMurray, R. J.; Gadegaard, N.; Tsimbouri, P. M.; Burgess, K. V.; McNamara, L. E.; Tare, R.; Murawski, K.; Kingham, E.; Oreffo, R. O.; Dalby, M. J. Nanoscale Surfaces for the Long-Term Maintenance of Mesenchymal Stem Cell Phenotype and Multipotency. *Nat. Mater.* **2011**, *10* (8), 637−644.

(16) Mirzaali, M.; Van Dongen, I.; Tümer, N.; Weinans, H.; Yavari, S. A.; Zadpoor, A. In-Silico Quest for Bactericidal but Non-Cytotoxic Nanopatterns. *Nanotechnology* **2018**, *29* (43), 43LT02.

(17) Widyaratih, D.; Hagedoorn, P.-L.; Otten, L.; Ganjian, M.; Tumer, N.; Apachitei, I.; Hagen, C. W. K.; Fratila-Apachitei, L.; Zadpoor, A. A. Towards Osteogenic and Bactericidal Nanopatterns? *Nanotechnology* **2019**, *30*, 20LT01.

(18) Tang, W.; Lin, D.; Yu, Y.; Niu, H.; Guo, H.; Yuan, Y.; Liu, C. Bioinspired Trimodal Macro/Micro/Nano-Porous Scaffolds Loading rhBMP-2 for Complete Regeneration of Critical Size Bone Defect. *Acta Biomater.* **2016**, *32*, 309−323.

(19) Roosa, S. M. M.; Kemppainen, J. M.; Moffitt, E. N.; Krebsbach, P. H.; Hollister, S. J. The Pore Size of Polycaprolactone Scaffolds has Limited Influence on Bone Regeneration in an In Vivo Model. *J. Biomed. Mater. Res., Part A* **2010**, *92A* (1), 359−368.

(20) Zorlutuna, P.; Annabi, N.; Camci-Unal, G.; Nikkhah, M.; Cha, J. M.; Nichol, J. W.; Manbachi, A.; Bae, H.; Chen, S.; Khademhosseini, A. Microfabricated Biomaterials for Engineering 3D Tissues. *Adv. Mater.* **2012**, *24* (14), 1782−1804.

(21) Zadpoor, A. A.; Malda, J. Additive Manufacturing of Biomaterials, Tissues, and Organs. *Ann. Biomed. Eng.* **2017**, *45*, 1−11.

(22) Zhang, S.; Vijayavenkataraman, S.; Lu, W. F.; Fuh, J. Y. A Review on the Use of Computational Methods to Characterize, Design, and Optimize Tissue Engineering Scaffolds, with a Potential in 3D Printing Fabrication. *J. Biomed. Mater. Res., Part B* **2019**, *107* (5), 1329−1351.

(23) Van der Stok, J.; Van der Jagt, O. P.; Amin Yavari, S.; De Haas, M. F.; Waarsing, J. H.; Jahr, H.; Van Lieshout, E. M.; Patka, P.; Verhaar, J. A.; Zadpoor, A. A. Selective Laser Melting-Produced Porous Titanium Scaffolds Regenerate Bone in Critical Size Cortical Bone Defects. *J. Orthop. Res.* **2013**, *31* (5), 792−799.

(24) Bsat, S.; Yavari, S.; Munsch, M.; Valstar, E.; Zadpoor, A. Effect of Alkali-Acid-Heat Chemical Surface Treatment on Electron Beam Melted Porous Titanium and its Apatite Forming Ability. *Materials* **2015**, *8* (4), 1612−1625.

(25) Jordahl, J. H.; Solorio, L.; Sun, H.; Ramcharan, S.; Teeple, C. B.; Haley, H. R.; Lee, K. J.; Eyster, T. W.; Luker, G. D.; Krebsbach, P. H. 3D Jet Writing: Functional Microtissues Based on Tessellated Scaffold Architectures. *Adv. Mater.* **2018**, *30* (14), 1707196.

(26) Mirzaali, M.; Edens, M.; de la Nava, A. H.; Janbaz, S.; Vena, P.; Doubrovski, E.; Zadpoor, A. Length-Scale Dependency of Biomimetic Hard-Soft Composites. *Sci. Rep.* **2018**, *8* (1), 12052.

(27) Mirzaali, M. J.; Nava, A. H. d. l.; Gunashekar, D.; Nouri-Goushki, M.; Doubrovski, E.; Zadpoor, A. A. Fracture Behavior of Bio-Inspired Functionally Graded Soft-Hard Composites Made by Multi-Material 3D Printing: The Case of Colinear Cracks. *Materials* **2019**, *12* (17), 2735.

(28) Vijayavenkataraman, S.; Zhang, L.; Zhang, S.; Hsi Fuh, J. Y.; Lu, W. F. Triply Periodic Minimal Surfaces Sheet Scaffolds for Tissue Engineering Applications: An Optimization Approach toward Biomimetic Scaffold Design. *ACS Appl. Bio Mater.* **2018**, *1* (2), 259−269.

(29) Janbaz, S.; Noordzij, N.; Widyaratih, D. S.; Hagen, C. W.; Fratila-Apachitei, L. E.; Zadpoor, A. A. Origami Lattices with Free-Form Surface Ornaments. *Sci. Adv.* **2017**, *3* (11), No. eaao1595.

(30) Brodoceanu, D.; Kraus, T. Micro-and Nanopatterning of Biomaterial Surfaces. In *Biomaterial Surface Science*; **2013**; Chapter 10, pp 285−309.

(31) Emons, M.; Obata, K.; Binhammer, T.; Ovsianikov, A.; Chichkov, B. N.; Morgner, U. Two-Photon Polymerization Technique with Sub-50 nm Resolution by Sub-10 fs Laser Pulses. *Opt. Mater. Express* **2012**, *2* (7), 942−947.

(32) Weiß, T.; Hildebrand, G.; Schade, R.; Liefeith, K. Two-Photon Polymerization for Microfabrication of Three-Dimensional Scaffolds for Tissue Engineering Application. *Eng. Life Sci.* **2009**, *9* (5), 384−390.

(33) Gross, A. J.; Bertoldi, K. Additive Manufacturing of Nanostructures That Are Delicate, Complex, and Smaller than Ever. *Small* **2019**, *15*, 1902370.

(34) Wang, S.; Yu, Y.; Liu, H.; Lim, K. T.; Srinivasan, B. M.; Zhang, Y. W.; Yang, J. K. Sub-10-nm Suspended Nano-Web Formation by Direct Laser Writing. *Nano Futures* **2018**, *2* (2), 025006.

(35) Nouri-Goushki, M.; Sharma, A.; Sasso, L.; Zhang, S.; Van der Eerden, B. C.; Staufer, U.; Fratila-Apachitei, L. E.; Zadpoor, A. A. Submicron Patterns-on-a-Chip: Fabrication of a Microfluidic Device Incorporating 3D Printed Surface Ornaments. *ACS Biomater. Sci. Eng.* **2019**, *5* (11), 6127−6136.

(36) Barlet, M.; Delaye, J.-M.; Charpentier, T.; Gennisson, M.; Bonamy, D.; Rouxel, T.; Rountree, C. L. Hardness and Toughness of Sodium Borosilicate Glasses via Vickers's Indentations. *J. Non-Cryst. Solids* **2015**, *417*, 66−79.

(37) Nielsen, L. E.; Landel, R. F. *Mechanical Properties of Polymers and Composites*, 2nd ed.; Marcel Dekker: New York, NY, USA, 1994.

DOI: 10.1021/acsami.9b17425
ACS Appl. Mater. Interfaces 2020, 12, 200−208

(38) Quéré, D. Wetting and Roughness. *Annu. Rev. Mater. Res.* **2008**, *38*, 71−99.
(39) Vereecke, G.; Xu, X.; Tsai, W.-K.; Yang, H.; Armini, S.; Delande, T.; Doumen, G.; Kentie, F.; Shi, X.; Simms, I. Wetting Behavior of Aqueous Solutions on High Aspect Ratio Nanopillars with Hydrophilic Surface Finish. *ECS Trans.* **2013**, *58* (6), 171−182.
(40) Courbin, L.; Denieul, E.; Dressaire, E.; Roper, M.; Ajdari, A.; Stone, H. A. Imbibition by Polygonal Spreading on Microdecorated Surfaces. *Nat. Mater.* **2007**, *6* (9), 661−664.
(41) Engler, A. J.; Sen, S.; Sweeney, H. L.; Discher, D. E. Matrix elasticity directs stem cell lineage specification. *Cell* **2006**, *126* (4), 677−689.
(42) Goushki, M. N.; Mousavi, S. A.; Abdekhodaie, M. J.; Sadeghi, M. Free Radical Graft Polymerization of 2-Hydroxyethyl Methacrylate and Acrylic Acid on the Polysulfone Membrane Surface Through Circulation of Reaction Media to Improve its Performance and Hemocompatibility Properties. *J. Membr. Sci.* **2018**, *564*, 762−772.
(43) Ranella, A.; Barberoglou, M.; Bakogianni, S.; Fotakis, C.; Stratakis, E. Tuning Cell Adhesion by Controlling the Roughness and Wettability of 3D Micro/Nano Silicon Structures. *Acta Biomater.* **2010**, *6* (7), 2711−2720.
(44) Yang, S. Y.; Kim, E.-S.; Jeon, G.; Choi, K. Y.; Kim, J. K. Enhanced Adhesion of osteoblastic Cells on Polystyrene Films by Independent Control of Surface Topography and Wettability. *Mater. Sci. Eng., C* **2013**, *33* (3), 1689−1695.

DOI: 10.1021/acsami.9b17425
ACS Appl. Mater. Interfaces 2020, 12, 200−208